

Simulation and TWINS observations of the 22 July 2009 storm

M.-C. Fok,¹ N. Buzulukova,¹ S.-H. Chen,¹ P. W. Valek,^{2,3} J. Goldstein,^{2,3}
and D. J. McComas^{2,3}

Received 8 March 2010; revised 31 August 2010; accepted 9 September 2010; published 14 December 2010.

[1] TWINS is the first mission to perform stereo imaging of the Earth's ring current. The magnetic storm on 22 July 2009 was at the time the largest storm observed since TWINS began routine stereo imaging in June 2008. On 22 July 2009, the *Dst* dropped to nearly -80 nT at 0700 and 1000 UT. During the main phase, and at the peak of the storm, TWINS 1 and 2 were near apogee and moving between predawn and postdawn local time. The energetic neutral atom (ENA) imagers on the two spacecraft captured the storm intensification and the formation of the partial ring current. The peak of the high-altitude ENA emissions was seen in the midnight-to-dawn local time sector. The development of this storm has been simulated using the comprehensive ring current model (CRCM) to understand and interpret the observed signatures. We perform CRCM runs with constant and time-varying magnetic field. The model calculations are validated by comparing the simulated ENA and ion flux intensities with TWINS ENA images and in situ ion data from a THEMIS satellite. Simulation with a static magnetic field produces a strong shielding electric field that skews the ion drift trajectories toward dawn. The model's corresponding peak ENA emissions are always more eastward than those in the observed TWINS images. On the other hand, the simulation with a dynamic magnetic field gives better spatial agreement with both ENA and in situ particle data, suggesting that temporal variations of the geomagnetic field exert a significant influence upon global ring current ion dynamics.

Citation: Fok, M.-C., N. Buzulukova, S.-H. Chen, P. W. Valek, J. Goldstein, and D. J. McComas (2010), Simulation and TWINS observations of the 22 July 2009 storm, *J. Geophys. Res.*, 115, A12231, doi:10.1029/2010JA015443.

1. Introduction

[2] The Two Wide-angle Imaging Neutral-atom Spectrometers (TWINS) mission is a NASA Explorer Mission of Opportunity to stereoscopically image the magnetosphere for the first time. TWINS 1 and 2 instruments fly on host spacecraft in Molniya orbits at 63.4° inclination with apogees of $7.2 R_E$ and perigees of 1000 km altitude, respectively. The orbit period is about 12 h. TWINS began its full science operation in June 2008 and since then it has been nearly continuously providing stereo images of the magnetosphere. Both TWINS 1 and 2 are equipped with an energetic neutral atom (ENA) imager and a Lyman-alpha detector. The instruments are mounted on rotating actuators to achieve broad, roughly nadir-centered viewing [McComas *et al.*, 2009].

[3] ENAs are created when energetic ions charge exchange with ambient neutral atoms [Roelof, 1987]. ENA imaging is a powerful tool to reveal the temporal and spatial development of the ring current, plasma sheet and ion

precipitation [Roelof *et al.*, 1985; Roelof, 1997; Fok *et al.*, 2003; Scime *et al.*, 2002; McComas *et al.*, 2002]. The TWINS Lyman-alpha detectors measure radiations produced by resonant scattering of solar Lyman α from exospheric neutral H. Techniques have been developed to derive neutral H density profiles from these geocoronal emissions [Rairden *et al.*, 1986; Østgaard *et al.*, 2003]. Accurate measurements of the H density profiles are crucial in ENA image inversion to quantitatively recover the ion distributions.

[4] The first ENA image of the ring current was captured by the ISEE 1 satellite during the main phase of the geomagnetic storm on 29 September 1978 [Roelof, 1987; Roelof and Williams, 1988]. This image showed a strong day-night asymmetry of the storm time ring current. ENA emissions from the ring current were also observed by the Polar satellite [Henderson *et al.*, 1997; Reeves and Henderson, 2001]. Reeves and Henderson analyzed the composite ENA images during isolated and storm time ion injections. They found the two types of injection differed primarily in local time extent and particle intensity. For isolated injections, ENA fluxes exhibited westward drift and dispersion, while during storm time injections, fluxes expanded eastward as well as westward to encompass most of the night-side. Moreover, ENA intensities during storm time injections were stronger and stayed elevated for longer periods of time than those at isolated injections.

¹NASA Goddard Space Flight Center, Greenbelt, Maryland, USA.

²Southwest Research Institute, San Antonio, Texas, USA.

³Department of Physics and Astronomy, University of Texas at San Antonio, San Antonio, Texas, USA.

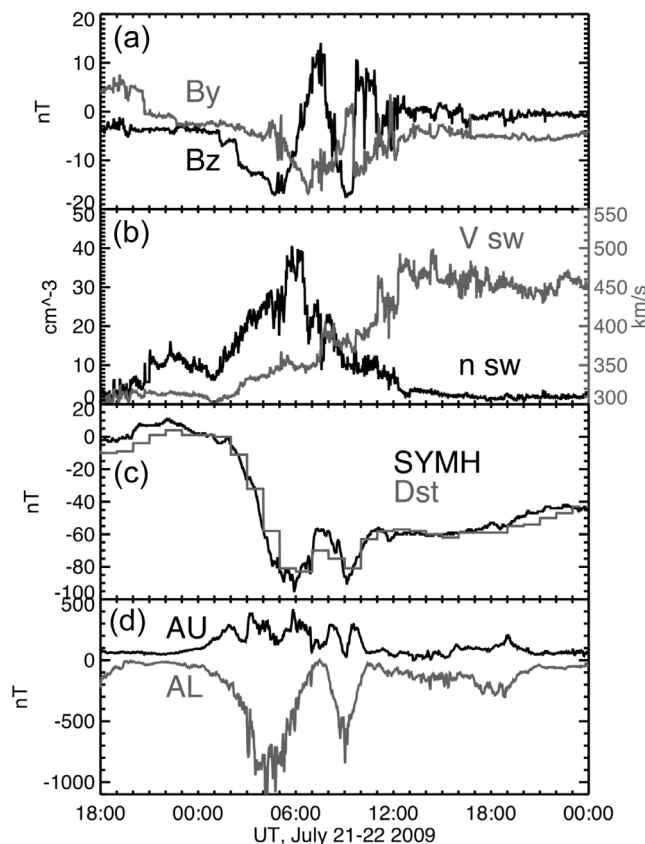


Figure 1. Solar wind parameters and geomagnetic indices during the storm on 22 July 2009. (a, b) Solar wind parameters are shifted from ACE satellite to the bow shock.

[5] The Image for Magnetopause-to-Aurora Global Exploration (IMAGE) was the first mission that carried dedicated ENA imagers to study the global structure and dynamics of the ring current [Burch, 2000; Mitchell *et al.*, 2000; Pollock *et al.*, 2000]. Mitchell *et al.* [2003] examined the temporal variations of H and O ENA images from the high-energy neutral atom (HENA) imager on IMAGE during storms. They observed that the increase in O ENA intensity was well correlated with the auroral substorm onset. Pollock *et al.* [2003] analyzed ENA images of low- and high-energy H^+ during to storm on 10 June 2000. They found low-energy H^+ drift slower and decay faster than higher-energy H^+ . The estimated drift velocity and loss rate were consistent with theoretical calculations. C:son Brandt *et al.* [2002] studied the local time distribution of HENA emissions during several storms. They noticed that the peak of ENA intensity shifted eastward to dawn with increasing interplanetary magnetic field (IMF) B_y . Later studies by Fok *et al.* [2003] and Ebihara and Fok [2004] confirmed that skewed electric fields caused the postmidnight enhancement of ring current ions. A strong shielding field, generated by the storm time ring current, is the main source that twists the potential contours eastward and thus alters the ion flow pattern.

[6] TWINS began routine stereo imaging in June 2008 during the deep minimum of solar cycle 23. The Sun was very quiet and so was the geomagnetic activity. However,

recurring high-speed solar wind streams can trigger substorm injections and particle acceleration even during minimum solar condition [Baker *et al.*, 1998]. On 22 July 2009, strong southward IMF of ~ 20 nT and increased solar wind density reached the Earth, followed by a high-speed stream. The magnetosphere responded with substorm and storm signatures, where AL attained a value ~ 1000 nT at 0400 UT and Dst of -79 nT at 1000 UT. This was the largest storm in years 2008 and 2009. Figure 1 shows the solar wind B_y , B_z , speed and density measured by the ACE satellite, and geomagnetic indices $symH$, Dst , AU , and AL on 22 July 2009. The solar wind parameters have been shifted to the bow shock by omniweb (<http://omniweb.gsfc.nasa.gov/html/HROddocum.html>). During the main and recovery phases of the storm, either TWINS 1 or 2 was near apogee and moving from predawn to postdawn local time. The ENA imagers on the two spacecraft captured the storm intensification and the formation of the partial ring current. The peak of the ENA emissions was seen in the midnight-to-dawn sector. An in depth report and analysis of TWINS observations on 22 July 2009 are presented by Valek *et al.* [2010].

[7] In order to better understand and interpret the observed signatures from TWINS ENA images on 22 July 2009, we simulated the development of this storm using the comprehensive ring current model (CRCM) [Fok *et al.*, 2001]. In the following, we present a brief description of the CRCM and model setup to calculate the ring current ion distribution. The simulated ENA and ion flux intensities are then compared with TWINS images and in situ ion data from THEMIS (Time History of Events and Macroscale Interactions during Substorms) satellites [Angelopoulos, 2008; Sibeck and Angelopoulos, 2008]. Finally, we discuss how the shielding field produced by the ring current and the effect of magnetosphere-ionosphere (M-I) coupling influence the structure and dynamics of the storm time ring current.

2. Model the 22 July 2009 Storm With the Comprehensive Ring Current Model

2.1. The Comprehensive Ring Current Model (CRCM)

[8] The comprehensive ring current model (CRCM) combines the Rice Convection Model (RCM) [Harel *et al.*, 1981] and the Fok ring current model [Fok and Moore, 1997]. To couple with the Fok model, the RCM algorithm for calculating Region 2 currents has been generalized to arbitrary pitch angle distribution [Fok *et al.*, 2001]. Two main equations are solved in the CRCM: (1) the kinetic equation of ring current ion distribution functions, and (2) the equation of ionospheric potential,

$$\frac{\partial f_s}{\partial t} + \langle \mathbf{v}_s \rangle \cdot \frac{\partial f_s}{\partial \mathbf{r}} = \left(\frac{\delta f_s}{\delta t} \right)_{\text{charge-exchange}} + \left(\frac{\delta f_s}{\delta t} \right)_{\text{loss-cone}} \quad (1)$$

$$\nabla \cdot \left(-\vec{\Sigma} \cdot \nabla \Phi \right) = J_{\parallel} \sin I \quad (2)$$

where f_s is phase space density of ring current species s and $\langle \mathbf{v}_s \rangle$ is the bounce-averaged drift velocity. The right-hand side of equation (1) represents charge exchange and loss

cone losses. Particles in the loss cone, which is set at 120 km altitude, will experience collisions with the atmosphere and the lifetimes are assumed to be one half of the bounce periods. In equation (2), Φ is potential at the ionosphere; Σ is a conductance tensor; J_{\parallel} is the field aligned current and I is the magnetic dip angle at the ionosphere.

[9] In this study, we use the magnetic configuration modeled by the Tsyganenko 1996 (T96) model [Tsyganenko and Stern, 1996]. The ring current H^+ and e^- are considered and charge exchange losses are applied to ions only. CRCM calculations are started at 1800 UT on the previous day (21 July) with an empty magnetosphere. The boundary distribution on the nightside at 10 R_E equator is assumed to be Maxwellian with ion temperature and density given by the model of Tsyganenko and Mukai [2003]. Electrons are assumed to have the same density as the ions at the boundary but their temperature is lower by a factor of 7.8 ($T_e = T_i/7.8$) [Baumjohann et al., 1989]. The conductance tensor in equation (2) superimposes an auroral enhancement of Hardy et al. [1987] on a background conductance based on models of the atmosphere, ionosphere and collision frequency [Hedin, 1991; Bilitza et al., 1993; Riley, 1994]. The potential at the poleward boundary is given by the Weimer model [Weimer, 2001]. With specifications of the magnetic field, initial and boundary particle distributions, and electric potential at the polar cap, the CRCM calculates the three-dimensional particle distributions in the inner magnetosphere, and Region 2 currents and potentials in the subauroral ionosphere.

2.2. CRCM Simulation of the Storm on 22 July 2009

[10] We have performed two CRCM runs. In the first (Run 1) the magnetic field is constant over time. We use the T96 model with parmod (1:4) = 1.2, -30, 0, -3. Note that parmod (1:4) in T96 correspond to solar wind dynamic pressure in nPa, Dst , IMF By and Bz in nT, respectively [Tsyganenko, 1995]. In the second (Run 2) we update the magnetic configuration every 5 min with parmod(1:4) specified according to the time-shifted solar wind parameters from the ACE satellite and Dst index from the World Data Center for Geomagnetism, Kyoto, Japan. In Run 2, the effects of inductive electric field because of time-varying magnetic field are thus taken into account. We have assumed that field lines are rooted at the ionosphere, so that the inductive electric field there is zero. However, the shapes of field lines at higher altitudes vary as a function of time according to parmod(1:4). If field lines are perfect conductors in which the potential is constant along a magnetic field line, the field line motion at high altitudes, e.g., at the equator, will generate an induction electric field of the form [Fok et al., 2005; Wolf et al., 2007],

$$\mathbf{E}_{\text{ind}} = -\mathbf{v}_o \times \mathbf{B}_o \quad (3)$$

where \mathbf{v}_o and \mathbf{B}_o are the field line velocity and magnetic field at the equator.

[11] In the top panel of Figure 2, Dst , symH, and symH* are depicted. The lower panels of Figure 2 show equatorial ion pressure and H^+ flux at 12 keV from Run 1 with fixed B field (Figures 2a and 2b) and Run 2 with time-varying B (Figures 2c and 2d). The white circles on the equatorial plots are geosynchronous orbits. The observed symH* is esti-

mated from the symH index as follow [Burton et al., 1975; Gonzalez et al., 1994; Kozyra et al., 2002]:

$$\text{symH}^* = \text{symH}/1.5 - 0.2P^{1/2} + 20 \quad (4)$$

where P is the solar wind dynamic pressure in $\text{eV} \cdot \text{cm}^{-3}$. The correction is performed to eliminate effects other than the ring current on the symH index.

[12] In Figure 2a, the calculated pressure from Run 1 is shown at times marked by vertical bars in the symH plot. At 0320 UT, the ion pressure peak is located at $\sim 6.5 R_E$ in the dusk-midnight sector; the storm continues to intensify. At 0455 UT, a high-pressure region extends in both local time and radial directions. The storm has a brief recovery at ~ 0600 to 0800 UT because of the northward turning of the IMF and the corresponding decrease in the convection strength. Some particles which are originally in open drift paths may find themselves drifting in closed paths. As a result, at 0820 UT, ion pressure disperses to the dayside and becomes more symmetric in local time. Then the second injection starts as the IMF turns southward again. At 0905 UT, strong pressure is seen on the nightside well inside the geosynchronous orbit. Then the abrupt IMF northward turning triggers a rapid symmetrization of ion distribution in local time, as seen in the pressure plot at 0955 UT. The storm then enters into a slow and long recovery. At 1705 UT, the CRCM predicts a typical quiet time symmetric ring current with the peak pressure located at $\sim 5 R_E$.

[13] Ions with particular energies behave differently from the overall pressure (1–180 keV). Figure 2b shows the calculated equatorial H^+ flux at 6–18 keV from Run 1 during the times marked in the Dst plot. The 12 keV (6–18 keV) ions exhibit temporal evolution similar to the pressure, showing enhancements during storm injections and significant decrease in intensity at late recovery. On the other hand, there are noticeable differences in spatial structures between pressure and the 12 keV ions. Relatively, the 12 keV ion fluxes peak near midnight to dawn but the pressure peaks in the dusk-midnight sector. This suggests that for this event the major contributors to the pressure are ions with higher energies whose fast westward magnetic drift bring the pressure peak to the premidnight sector. Another feature worth mentioning in the 12 keV ion flux is the localized deep earthward penetration near local dawn. Tip-like structures at dawn at the inner edge of the ring current are seen around the peak of the storm (times 2–5) when convection is strong. In this period of time, a robust ring current had been established and the associated shielding field twisted the potential pattern eastward near dawn [Wolf, 1974; Fok et al., 2003; Ebihara and Fok, 2004]. This flux incursion of tens of keV ions can be found in both major and moderate storms [Buzulukova et al., 2010]. Figure 3a plots the calculated convection potentials at the equator at 0455 UT. Contours are 4 kV apart. The skewing of potential contours near dawn is clearly seen. In Figure 3b we plot the drift trajectories of equatorially mirroring ions with magnetic moment of 10^7 keV/T, assuming a static convection field. Ion energy at 0500 MLT at 3 R_E is 12 keV. Figure 3b shows that ions convecting inward from midnight would turn eastward toward dawn. This drift pattern does not produce exactly the spatial structure in Figure 2a because the convection field is not static in the CRCM run. However, it

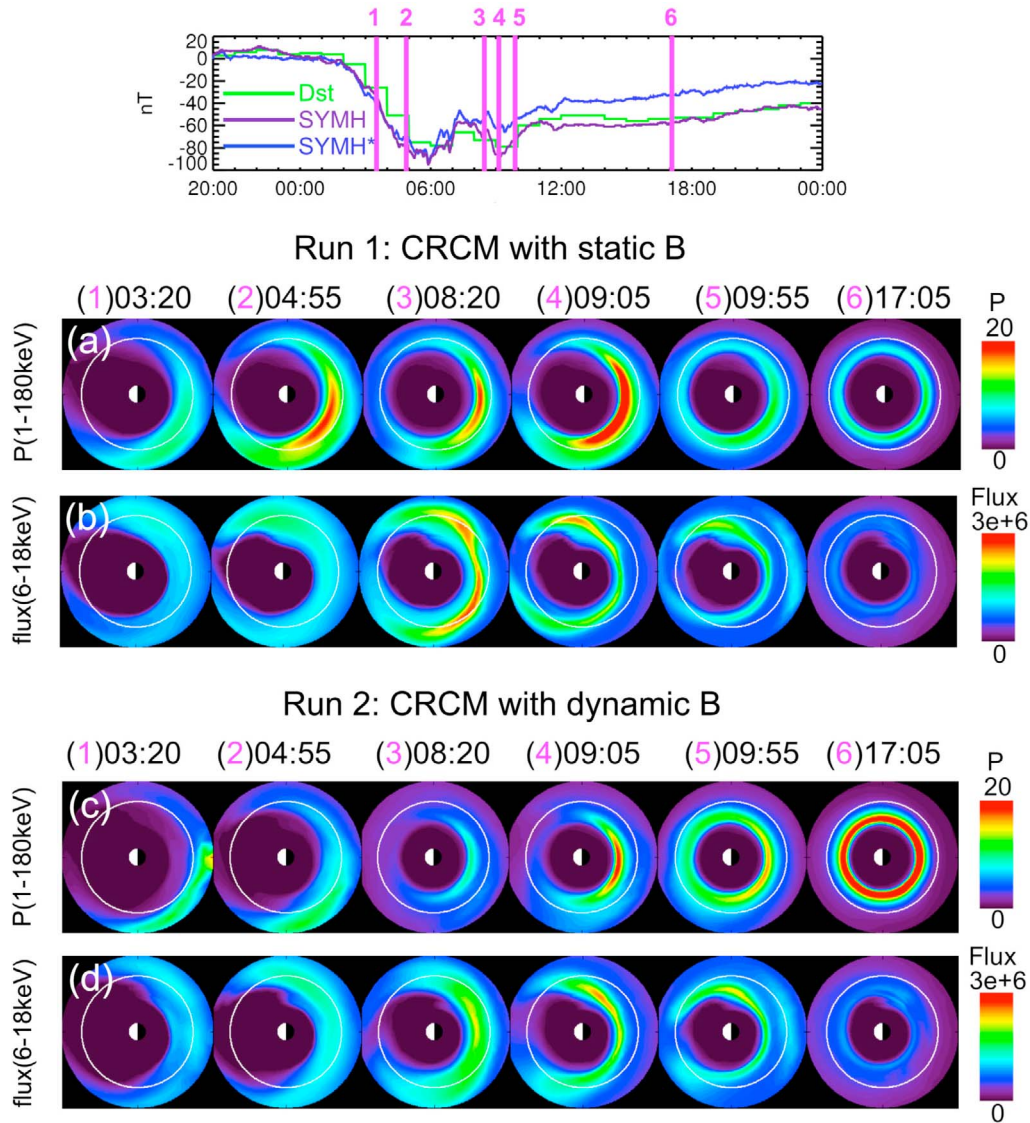


Figure 2. (top) *Dst* (green), *symH* (purple), and *symH** (blue). (a–d) CRCM simulation results of the storm on 22 July 2009 at times marked by the magenta lines in the top panel. Figures 2a and 2b show calculated ion pressure in nPa and 6–18 keV H^+ flux in $\text{cm}^{-2}\text{s}^{-1}\text{sr}^{-1}\text{keV}^{-1}$, respectively. Figures 2c and 2d have the same format as Figures 2a and 2b except for Run 2 with dynamic B.

provides clues about the predawn flux enhancement of tens of keV ions. This localized ion peak near the Earth has no major effect on the total pressure (Figure 2b), however, it could be significant in ENA emissions. The charge exchange rate and thus ENA production is proportional to neutral density, which increases rapidly with decreasing distance from the Earth.

[14] Returning to Figure 2, the lower half of the figure shows CRCM results from Run 2 in which the magnetic field is updated every 5 min. The spatial structure of the ion pressure (Figure 2c) is very different from those in Run 1. At 0320 and 0455 UT during ion injections, the strong ion pressure is located further away from the Earth and more toward the dusk-midnight sector. At 0820 UT, the CRCM predicts a more deeply penetrating but weaker ring current.

At 0905 UT, the calculated ion pressure increases in magnitude, local time and radial extent. High ion pressure then expands to all local times at 0955 UT. At the storm's late recovery at 1705 UT, Run 2 predicts deep earthward penetration of ions and a much stronger ion pressure when compared with that in Run 1. We find that these deeply penetrating particles are ions with a mean energy of ~ 50 keV. The inductive electric field associated with fluctuating magnetic fields enhances the radial transport of ions, especially high-energy ions [Chen *et al.*, 1993]. Figure 2d plots the 12 keV H^+ fluxes from Run 2. Similar to the case of static magnetic field, the calculated fluxes from Run 2 peak in the midnight-dawn sector during the main and early recovery phases and become symmetric in local time at 1705 UT. However, the predawn enhancement near the

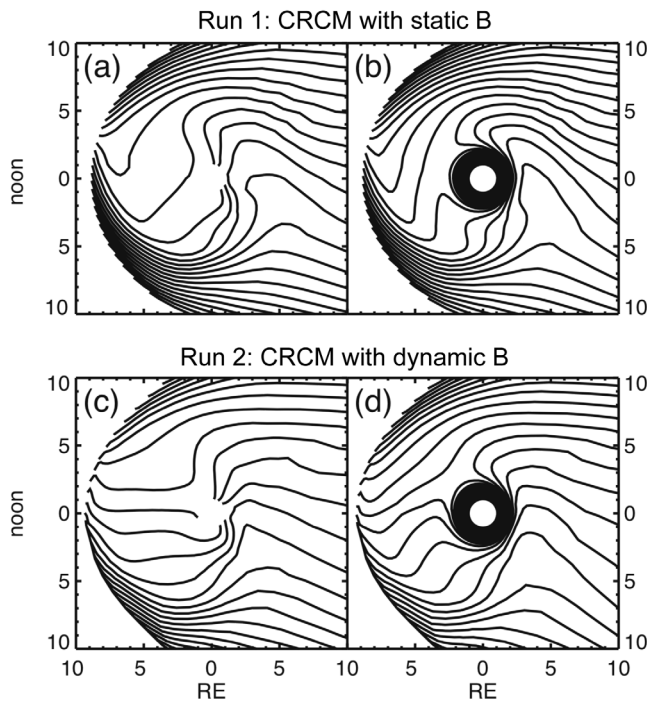


Figure 3. (a, c) CRCM calculated potentials at 0455 UT on 22 July 2009. (b, d) Calculated drift paths at the same time of equatorially mirroring ions with magnetic moment of 10^7 keV/T.

Earth is just barely seen at 0455 UT and disappears at later times. Figure 3c shows the CRCM potential at 0455 UT from Run 2. When compared with Run 1, this run predicts a less twisted potential pattern. The weaker ring current produced in Run 2 at 0455 UT results in weaker shielding and thus less eastward skewing of the potential contours. The drift paths of equatorially mirroring ions with magnetic moment of 10^7 keV/T are plotted in Figure 3d. The

dawnward movement of ions is again evident. However, in Run 2, both convection and magnetic field are varied with time. The skewing effect is smoothed out in the fluctuating fields and thus the dawn “tip” is only barely seen at 0455 UT.

3. TWINS Observations of the Storm on 22 July 2009

[15] Both TWINS 1 and 2 were operated normally on 22 July 2009. They are in orbits roughly 90° apart with apogees that straddle dawn local time. The large orbit phase offset between TWINS 1 and 2 allows continuous monitoring of the storm at high altitude (see also *Valek et al.* [2010]). This full coverage of storm development was not previously done by single-spacecraft missions, such as IMAGE. Figure 4a plots the ENA images of 6–18 keV taken from TWINS 1 (TW1) and TWINS 2 (TW2) at the same times as in Figure 2. Each image is composed of data averaged over 10 sweeps of ~ 15 min accumulation time. The limb of the Earth and dipole field lines of $L = 4$ and 8 at four magnetic local times are drawn as spatial references; field lines at noon are colored in red and dusk field lines in magenta. The bow tie-like strong emission at 0455 UT is an internal scattering effect of the intense low-altitude ENAs [*Valek et al.*, 2010]. Figure 4a shows that TWINS 1 and 2 capture the storm growth from 0320 to 0455 UT, the brief recovery at 0820 UT, the second intensification at 0905 and 0955 UT, and the late recovery at 1705 UT. Low-altitude emissions (LAE) are seen early on the day and fade away at 0955 UT while high-altitude ring current emissions (RCE) are still prominent. The leading of LAE over RCE during storms and substorms has been previously observed and modeled [*Cson Brandt et al.*, 2002; *Fok et al.*, 2006]. LAE are generated by precipitating ions and ions with mirror points near the Earth. During storm and substorm injections, ions are transported earthward from the plasma sheet, from a region where they are mostly with isotropic to field-aligned

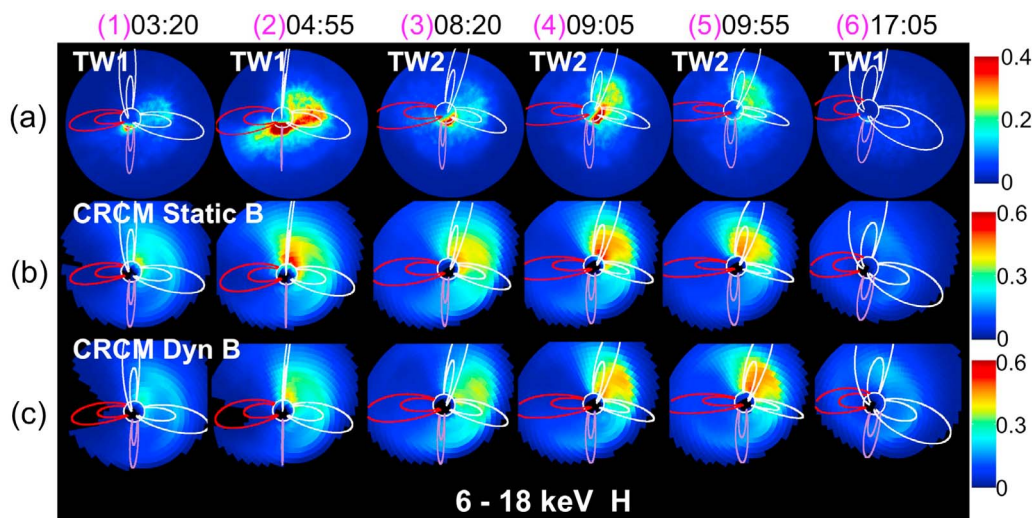


Figure 4. (top) Dst (green), $symH$ (purple), and $symH^*$ (blue). (a) TWINS 6–18 keV H fluxes in $\text{cm}^{-2}\text{s}^{-1}\text{sr}^{-1}\text{eV}^{-1}$ and (b–c) CRCM calculated images at the times marked by magenta bar in the top panel.

pitch angle distributions [Mauk and McIlwain, 1975; Mauk and Meng, 1986; Fok et al., 2006]. These freshly injected ions thus produce strong LAE. During the recovery phase, most of the field-aligned ions are already lost and a sharp decrease in LAE is expected. The trapped ring current ions with pitch angle near perpendicular direction are relatively long-lived and decay gradually into full recovery.

[16] As shown in Figure 4a, the RCE is strongest in the midnight-dawn sector. When the ring current is weak at times 1, 3, and 6, peak emissions are found closer to midnight. When the ring current is stronger at times 2, 4, and 5, higher intensity emissions extend to dawn local time. In order to understand the observed spatial structures and temporal variations of RCE, we calculate ENA emissions based on the CRCM 12 keV (6–18 keV) H^+ fluxes shown in Figure 2. Even though equatorial fluxes are plotted in Figure 2, the CRCM provides ion intensity and pitch angle distribution in three-dimensional space [Fok and Moore, 1997; Fok et al., 1995, 2001]. To simulate what TWINS would see, we perform line of sight integration from the TWINS position to the CRCM simulation domain boundary:

$$j_{\text{ENA}} = \int j_{\text{ion}} \sigma_{H,H^+} n_H dl \quad (5)$$

where j_{ion} is the H^+ differential flux output from the CRCM, n_H is H geocoronal density, and σ_{H,H^+} is the charge exchange cross section of H^+ ions with neutral H. We use the model of Rairden et al. [1986] for the neutral H density. In this study, we only consider the charge exchange interaction between ring current ions and the H geocorona. The contribution from the neutral oxygen is ignored. As a result, we underestimate the low-altitude emission. In the future, we will apply the thick-target technique [Bazell et al., 2010] to calculate emissions at low altitudes. For the present work we would focus on the high-altitude ring current emissions only.

[17] Figures 4b and 4c plot the CRCM 12 keV H ENA calculated from ion fluxes of Run 1 and Run 2 at the times when TWINS data are shown. Note that the color scales of the calculated ENA fluxes are not the same as scale for the TWINS data. As mentioned above, the ENA calculations exclude the contribution from neutral O, so the observed strong LAE at times 1–4 are not seen in the CRCM ENA images. However, the CRCM reproduces the two periods of storm intensification, and the brief recovery in between, as seen in the TWINS RCE data (Figure 4a). The model also predicts strong emission in the midnight-dawn sector at times 1–5 that is consistent with TWINS observations. When comparing results from the two CRCM simulations, Run 1 produces stronger ENA fluxes near the Earth at dawn at times 2–4. These localize emissions are mainly produced by the “tip” structure at dawn seen in the 12 keV H^+ flux (Figures 2b–4). Even though the ion flux intensities of the “tips” are low, the associated ENA emissions are high because of elevated neutral H densities at these altitudes. The “tip” structure is barely seen in the CRCM Run 2 (Figure 2d). As a result, the corresponding ENA emissions are relatively mild and smooth (Figure 4c).

[18] When comparing the simulated ENA images from the two CRCM runs with the TWINS images, the run with

dynamic magnetic field (Run 2) seems to agree with data better than the run with static magnetic field (Run 1). Run 1 produces strong emissions at dawn at times 2–5, which are not consistent with the observations. Relatively, ENA fluxes from Run 2 reproduce the peak location and local time extent of the TWINS images very well. This study has demonstrated the influences of magnetic field morphology and fluctuations on ring current structure and dynamics [Ebihara et al., 2008; Fok and Moore, 1998; Fok et al., 1999, 2006; Zaharia et al., 2006] and is consistent with the study by Wolf et al. [2007] that magnetic field variations can weaken the shielding effect by the ring current.

4. THEMIS-CRCM Comparison

[19] In situ measurements provide the “ground truth” of global modeling and imaging data [Vallat et al., 2004]. On 22 July 2009, both THEMIS-D and E satellites passed through the inner magnetosphere. The top panels of Figure 5 plot the orbit of THEMIS-D projected on SM X-Y, Y-Z and X-Z planes. It can be seen in the Figure 5 that the orbital planes are very close to the SM equator with apogee near 1600 MLT and perigee 0400 MLT. The solid state telescope (SST) and electrostatic analyzer (ESA) [Angelopoulos, 2008; McFadden et al., 2008] measure ion distribution functions in energy ranges of 5 eV to 25 keV (ESA) and 25 keV to 1 MeV (SST). Figure 5a plots the energy flux measured by ESA and SST on THEMIS-D (TH-D) from 0600–1700 UT on 22 July 2009. The SST instrument did not respond well at low energies, so there was a data gap from 20 to 30 keV in the spectrogram (Vassilis Angelopoulos, private communication, 2010).

[20] TH-D entered the magnetosphere at dusk local time, then passed through the inner magnetosphere on the night-side to the inner edge of the ring current. The peak flux during the inbound pass is at ~20 keV. A “nose” structure [Smith and Hoffman, 1974; Ejiri et al., 1980; Ganushkina et al., 2001; Buzulukova and Vovchenko, 2008] is seen at ~1015 UT showing the deep penetration 20 keV ions down to 2.5 R_E . On the outbound pass, a bite-out (labeled with a red arrow) at ~10 keV is seen at 0700 MLT. This is also a well observed signature often found in satellite energy-time spectrograms [McIlwain, 1972; Lennartsson et al., 1981; Buzulukova et al., 2002; Ebihara et al., 2004]. Ions of certain energies, experience eastward and westward drifts that are similar in magnitude, resulting in very slow drift velocity. The “hole” in the energy spectra corresponds to particles at these energies which have either not yet reached the observation point or which have experienced significant losses during their slow drift to the observation point. TH-D then continued to move through the core of the ring current to the dayside magnetopause.

[21] A relatively subtle signature is seen in the TH-D spectrogram (Figure 5a) between the two *Dst* minima at 0730–0900 UT. A substorm growth and then expansion were taking place during this time period as indicated from the AL index (Figure 1d) and from the GOES-11 magnetic field data (not shown). TH-D was moving in the dusk sector near the geosynchronous orbit at this time. A “negative slope” is found in the energy spectrogram, that is, flux drop out first seen at energy of ~20 keV and then particle injection during substorm expansion with lower-energy ions

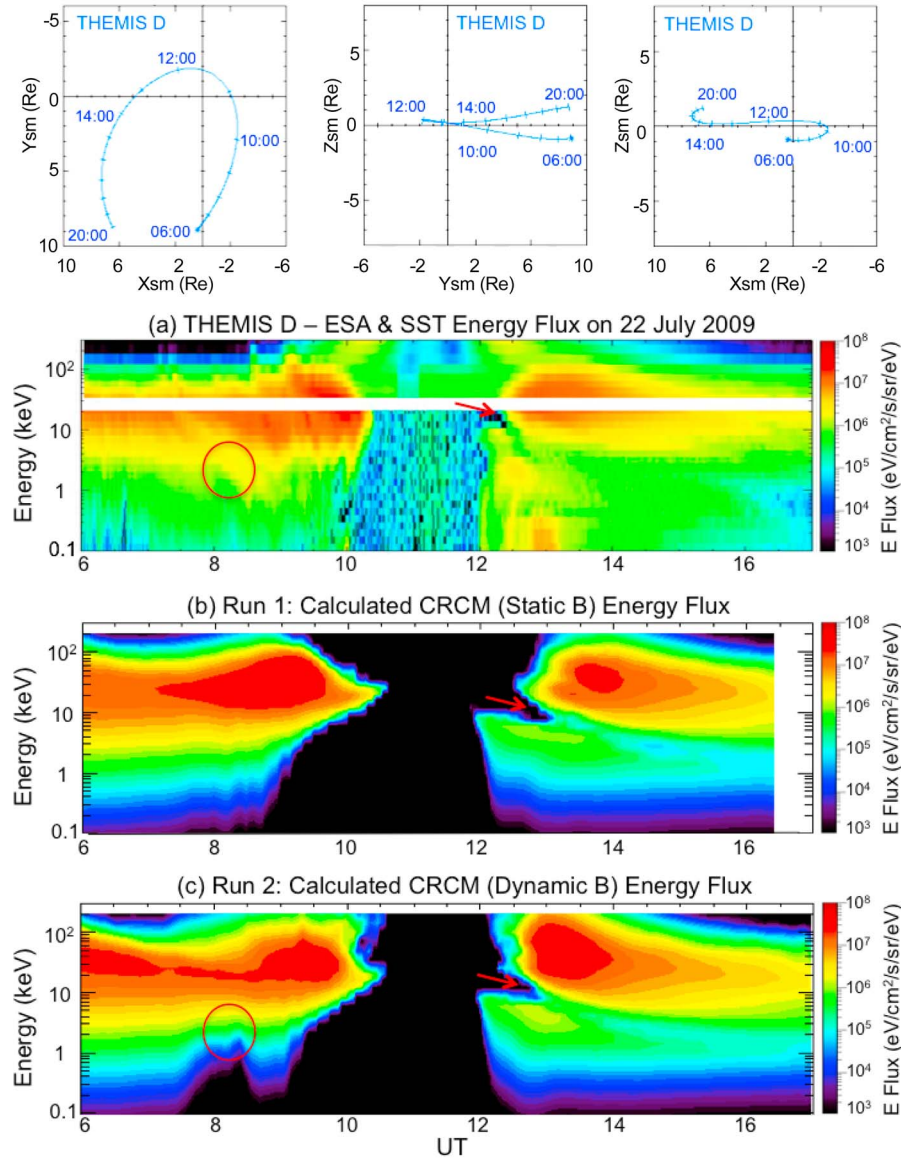


Figure 5. (top) The orbits of THEMIS D (blue) and E (red) projected on SM X-Y, Y-Z, and X-Z planes on 22 July 2009. (a) ESA and SST spectrogram from THEMIS-D. (b and c) CRCM calculated spectrogram from Run 1 and Run 2, respectively. Red arrows indicate the drift-holes in Figures 5a–5c.

led by higher-energy ones. This wedge structure is well known during substorm injections [DeForest and McIlwain, 1971; Mauk and Meng, 1983; Fok et al., 1999; Ebihara et al., 2001]. High-energy ions injected from midnight drift westward with high speed and reach the dusk observation point earlier than ions with lower energies.

[22] Next we examine how well the CRCM reproduces the features in the TH-D spectrogram. Figures 5b and 5c display the simulated energy spectra along the TH-D orbit on 22 July 2009. Both CRCM runs reproduced reasonably well the general structure of the TH-D spectrogram: energy of the peak flux, nose structure and drift hole. Run 1 predicts zero fluxes at all energies after 1650 UT when TH-D exited the T96 magnetopause of this particular run. Moreover, Run 1 predicts a larger flux drop out at the inner edge of the ring

current and a wider bite-out (red arrow) at the drift hole. Run 2 with dynamic magnetic field (Figure 5c), on the other hand, predicts a deeper penetration of the ring current that agrees better with the TH-D data. The drift-stagnation feature is also well reproduced. Run 2 also better reproduces the observed flux decrease followed by ion injection around 0800 UT at the time of substorm growth and expansion (red circles in Figures 5a and 5c). IMF B_z is going southward from 0800 to 0900 UT and then abruptly turning northward at 0900 UT (Figure 1a). In T96, the southward turning of IMF B_z produces a stretched magnetotail and northward turning results in a contracted (more dipolar) magnetotail. Run 2 with time-varying T96 thus in some degree mimics the substorm growth before 0800 UT and the subsequent expansion. Once again we have demonstrated that radial

transport associated with time-varying magnetic field is important in distributing particles in the inner magnetosphere. This is consistent with the previous study by Ganushkina *et al.* [2005, 2006] that substorm associated inductive electric field produces fast inward motion of nose structures.

[23] The low-energy (<500 eV) ions observed by TH-D, especially the high fluxes in the period of 1200 to 1400 UT are not seen in the CRCM simulations. Low-energy ions (a few 500 eV) have been observed in the inner magnetosphere [Lennartsson and Sharp, 1982; Horwitz *et al.*, 1982; Shelley *et al.*, 1985; Chen and Moore, 2006; Chappell *et al.*, 2008]. The source of this “warm” ion population is not definitely known yet. Nagai *et al.* [1983] suggested that these warm ions are auroral outflowing ions, which are heated and scattered in pitch angle so that they become trapped. From the results of their theoretical calculations, Fok *et al.* [1993] proposed that the storm time buildup of warm ions is a result of energy degradation of ring current ions caused by Coulomb collisions with the plasmasphere. Another suggested mechanism is circulation of ionospheric polar wind ions through the magnetosphere and their subsequent energization and contribution to the warm ions observed in the inner magnetosphere [Chappell *et al.*, 2008]. Our CRCM runs in this study consider neither of the above processes and thus we are not reproducing the high fluxes of low-energy ions seen by TH-D during the 22 July 2009 storm. However, inclusion of the low-energy ion sources will be pursued in our future investigations.

5. Discussion and Conclusions

[24] The magnetic storm on 22 July 2009 was the largest storm seen during the prolonged minimum of solar cycle 23. We have studied this storm by performing CRCM simulations and analyzing ENA data from TWINS and in situ ion data from THEMIS-D. The agreement between the model calculations and satellite observations is, in general, very good. The simulations are able to account for the postmidnight peak of 12 keV H ENAs, and the nose and drift-hole structures in the energy-time spectrogram.

[25] In general, CRCM Run 2 with the time varying magnetic field reproduces the observable signatures of the storm time ring current better than Run 1 with static field. However, Run 2 overestimates the earthward diffusion of high-energy (>50 keV) ions during the long recovery (Figure 5d). Also, the simulations fail to reproduce some small-scale structures seen in the THEMIS spectrogram. We plan to revisit this discrepancy using the CRCM coupled with a magnetohydrodynamics (MHD) model, in which the MHD model would provide global magnetic field, polar cap potential and ion distribution at the CRCM outer boundary in the plasma sheet. This approach will allow consistent treatment of the global magnetic reconfiguration and the density and temperature variations in the ring current source region [Keller *et al.*, 2005; Fok *et al.*, 2006; Moore *et al.*, 2008] and will hopefully allow an even more quantitative comparisons of the TWINS imaging data and model calculations.

[26] In this paper we use a spherically symmetric hydrogen density model [Rairden *et al.*, 1986] to calculate the ENA emissions. Previous studies have shown that exo-

sphere density can vary with latitude, local time, season and solar cycle [Hodges, 1994; Østgaard *et al.*, 2003]. As mentioned above, the TWINS LAD measures the Lyman- α resonance emissions and the global exospheric density can be derived from the LAD data [Zoennchen *et al.*, 2010]. In the future, we plan to use the TWINS-LAD derived neutral density to calculate the ENA emissions in order to reduce errors coming from simply using an average neutral model.

[27] In summary, we have performed two CRCM runs to study the storm on 22 July 2009: Run 1 with static magnetic field and Run 2 with time varying magnetic field. The simulation results are compared with TWINS ENA and THEMIS ion data. We found the following:

[28] 1. The shielding field in Run 1 is stronger than that in Run 2.

[29] 2. Run 1 produces more eastward skewing of potential lines than Run 2.

[30] 3. Run 2 produces better agreement of the flux intensity and local time distribution with TWINS 12 keV ENAs than Run 1.

[31] 4. The nose and drift-hole signatures seen in the THEMIS-D energy-time spectrogram are better reproduced by Run 2 than Run 1.

[32] We have demonstrated the importance of magnetic field fluctuations and the associated inductive electric field in controlling the ring current structure and dynamics. The inductive electric field plays a more vital role during moderate storms when convection is relatively modest. The magnetosphere shows much more small-scale complexity (e.g., THEMIS observations) than the models can account for, while TWINS ENA imaging provides the big picture. Ultimately it should be possible to use TWINS to further develop the modeling to expose what are local fluctuations versus global properties and structures.

[33] **Acknowledgments.** We gratefully acknowledge use of the ACE solar wind data provided through OMNI and THEMIS data from <http://themis.ssl.berkeley.edu/>. The *Dst* and *symH* data are provided by the World Data Center for Geomagnetism at Kyoto University, Japan. We thank Vasilis Angelopoulos for comments on the THEMIS data and providing software to remove background of the data. For Natalia Buzulukova, this work was supported by an appointment to the NASA Postdoctoral Program at the Goddard Space Flight Center, administered by Oak Ridge Associated Universities through a contract with NASA. We are indebted to all of the dedicated work of the TWINS team bringing these great stereo ENA images of the magnetosphere to reality. This work was supported by the TWINS mission as a part of NASA's Explorer Program, and by NASA Heliophysics Guest Investigators Program under Work Breakdown Structure 955518.02.01.02.57.

[34] Masaki Fujimoto thanks the reviewers for their assistance in evaluating this paper.

References

- Angelopoulos, V. (2008), The THEMIS mission, *Space Sci. Rev.*, **141**, 5–34, doi:10.1007/s11214-008-9336-1.
- Baker, D. N., T. I. Pulkkinen, X. Li, S. G. Kanekal, J. B. Blake, R. S. Selesnick, M. G. Henderson, G. D. Reeves, H. E. Spence, and G. Rostoker (1998), Coronal mass ejections, magnetic clouds, and relativistic magnetospheric electron events: ISTEP, *J. Geophys. Res.*, **103**, 17,279–17,291, doi:10.1029/97JA03329.
- Baumjohann, W., G. Paschmann, and C. A. Cattell (1989), Average plasma properties in the central plasma sheet, *J. Geophys. Res.*, **94**, 6597–6606, doi:10.1029/JA094iA06p06597.
- Bazell, D., E. Roelof, T. Sotirelis, P. C. Brandt, H. Nair, P. Valek, J. Goldstein, and D. McComas (2010), Comparison of TWINS images of low-altitude emissions of energetic neutral atoms emissions with

- DMSP precipitating ion fluxes, *J. Geophys. Res.*, **115**, A10204, doi:10.1029/2010JA015644.
- Bilitza, D., K. Rawer, L. Bosny, and T. Gulyaeva (1993), International reference ionosphere—Past, present, future: I. Electron density, *Adv. Space Res.*, **13**(3), 3–13, doi:10.1016/0273-1177(93)90240-C.
- Burch, J. L. (2000), IMAGE mission overview, *Space Sci. Rev.*, **91**, 1–14, doi:10.1023/A:1005245323115.
- Burton, R. K., R. L. McPherron, and C. T. Russell (1975), An empirical relationship between interplanetary conditions and *Dst*, *J. Geophys. Res.*, **80**, 4204–4214, doi:10.1029/JA080i031p04204.
- Buzulukova, N. Y., and V. Vovchenko (2008), Modeling of proton nose structures in the inner magnetosphere with a self-consistent electric field model, *J. Atmos. Sol. Terr. Phys.*, **70**, 503–510, doi:10.1016/j.jastp.2007.08.028.
- Buzulukova, N. Y., Y. I. Galperin, R. A. Kovrazhkin, A. L. Glazunov, G. A. Vladimirova, H. Stenuit, J. A. Sauvaud, and D. C. Delcourt (2002), Two types of ion spectral gaps in the quiet inner magnetosphere: Interball-2 observations and modeling, *Ann. Geophys.*, **20**, 349–364, doi:10.5194/angeo-20-349-2002.
- Buzulukova, N., M.-C. Fok, J. Goldstein, P. W. Valek, D. J. McComas, and P. C. Brandt (2010), Ring current dynamics in modest and strong storms: Comparative analysis of TWINS and IMAGE/HENA data with CRISM, *J. Geophys. Res.*, doi:10.1029/2010JA015292, in press.
- Chappell, C. R., M. M. Huddleston, T. E. Moore, B. L. Giles, and D. C. Delcourt (2008), Observations of the warm plasma cloak and an explanation of its formation in the magnetosphere, *J. Geophys. Res.*, **113**, A09206, doi:10.1029/2007JA012945.
- Cson Brandt, P., R. Demajistre, E. C. Roelof, S. Ohtani, D. G. Mitchell, and S. Mende (2002), IMAGE/high-energy energetic neutral atom: Global energetic neutral atom imaging of the plasma sheet and ring current during substorms, *J. Geophys. Res.*, **107**(A12), 1454, doi:10.1029/2002JA009307.
- Chen, M. W., M. Schulz, L. R. Lyons, and D. J. Gorney (1993), Stormtime transport of ring current and radiation belt ions, *J. Geophys. Res.*, **98**, 3835–3849, doi:10.1029/92JA02608.
- Chen, S.-H., and T. E. Moore (2006), Magnetospheric convection and thermal ions in the dayside outer magnetosphere, *J. Geophys. Res.*, **111**, A03215, doi:10.1029/2005JA011084.
- DeForest, S. E., and C. E. McIlwain (1971), Plasma clouds in the magnetosphere, *J. Geophys. Res.*, **76**, 3587–3611, doi:10.1029/JA076i016p03587.
- Ebihara, Y., and M.-C. Fok (2004), Postmidnight storm-time enhancement of tens-of-keV proton flux, *J. Geophys. Res.*, **109**, A12209, doi:10.1029/2004JA010523.
- Ebihara, Y., M. Yamauchi, H. Nilsson, R. Lundin, and M. Ejiri (2001), Wedge-like dispersion of sub-keV ions in the dayside magnetosphere: Particle simulation and Viking observation, *J. Geophys. Res.*, **106**, 29,571–29,584, doi:10.1029/2000JA000227.
- Ebihara, Y., M. Ejiri, H. Nilsson, I. Sandahl, M. Grande, J. F. Fennell, J. L. Roeder, D. R. Weimer, and T. A. Fritz (2004), Multiple discrete-energy ion features in the inner magnetosphere: 9 February 1998 event, *Ann. Geophys.*, **22**, 1297–1304, doi:10.5194/angeo-22-1297-2004.
- Ebihara, Y., M.-C. Fok, J. B. Blake, and J. F. Fennell (2008), Magnetic coupling of the ring current and the radiation belt, *J. Geophys. Res.*, **113**, A07221, doi:10.1029/2008JA013267.
- Ejiri, M., R. A. Hoffman, and P. H. Smith (1980), Energetic particle penetrations into the inner magnetosphere, *J. Geophys. Res.*, **85**, 653–663, doi:10.1029/JA085iA02p00653.
- Fok, M.-C., and T. E. Moore (1997), Ring current modeling in a realistic magnetic field configuration, *Geophys. Res. Lett.*, **24**, 1775–1778, doi:10.1029/97GL01255.
- Fok, M.-C., and T. E. Moore (1998), Drift-shell splitting in an asymmetric magnetic field, in *Geospace Mass and Energy Flow: Results From the ISTP Program*, *Geophys. Monogr. Ser.*, vol. 104, edited by J. L. Horwitz et al., pp. 327–331, AGU, Washington, D. C.
- Fok, M.-C., J. U. Kozyra, A. F. Nagy, C. E. Rasmussen, and G. V. Khazanov (1993), Decay of equatorial ring current ions and associated aeronomical consequences, *J. Geophys. Res.*, **98**, 19,381–19,393, doi:10.1029/93JA01848.
- Fok, M.-C., T. E. Moore, J. U. Kozyra, G. C. Ho, and D. C. Hamilton (1995), Three-dimensional ring current decay model, *J. Geophys. Res.*, **100**, 9619–9632, doi:10.1029/94JA03029.
- Fok, M.-C., T. E. Moore, and D. C. Delcourt (1999), Modeling of inner plasma sheet and ring current during substorms, *J. Geophys. Res.*, **104**, 14,557–14,569, doi:10.1029/1999JA000014.
- Fok, M.-C., R. A. Wolf, R. W. Spiro, and T. E. Moore (2001), Comprehensive computational model of the Earth's ring current, *J. Geophys. Res.*, **106**, 8417–8424, doi:10.1029/2000JA000235.
- Fok, M.-C., et al. (2003), Global ENA IMAGE simulations, *Space Sci. Rev.*, **109**, 77–103, doi:10.1023/B:SPAC.0000007514.56380.f0.
- Fok, M.-C., Y. Ebihara, T. E. Moore, D. M. Ober, and K. A. Keller (2005), Geospace storm processes coupling the ring current, radiation belt and plasmasphere, in *Inner Magnetosphere Interactions: New Perspectives From Imaging*, *Geophys. Monogr. Ser.*, vol. 159, edited by J. Burch et al., pp. 207–220, AGU, Washington, D. C.
- Fok, M.-C., T. E. Moore, P. C. Brandt, D. C. Delcourt, S. P. Slinker, and J. A. Fedder (2006), Impulsive enhancements of oxygen ions during substorms, *J. Geophys. Res.*, **111**, A10222, doi:10.1029/2006JA011839.
- Ganushkina, N. Y., et al. (2001), Formation of intense nose structures, *Geophys. Res. Lett.*, **28**, 491–494, doi:10.1029/2000GL011955.
- Ganushkina, N. Y., T. I. Pulkkinen, and T. Fritz (2005), Role of substorm-associated impulsive electric fields in the ring current development during storms, *Ann. Geophys.*, **23**, 579–591, doi:10.5194/angeo-23-579-2005.
- Ganushkina, N. Y., T. I. Pulkkinen, M. Liemohn, and A. Milillo (2006), Evolution of the proton ring current energy distribution during 21–25 April 2001 storm, *J. Geophys. Res.*, **111**, A11S08, doi:10.1029/2006JA011609.
- Gonzalez, W. D., J. A. Joselyn, Y. Kamide, H. W. Kroehl, G. Rostoker, B. T. Tsurutani, and V. M. Vasylunas (1994), What is a geomagnetic storm?, *J. Geophys. Res.*, **99**, 5771–5792, doi:10.1029/93JA02867.
- Hardy, D. A., M. S. Gussenhoven, R. Raistrick, and W. J. McNeil (1987), Statistical and functional representations of the pattern of auroral energy flux, number flux, and conductivity, *J. Geophys. Res.*, **92**, 12,275–12,294, doi:10.1029/JA092iA11p12275.
- Harel, M., R. A. Wolf, P. H. Reiff, R. W. Spiro, W. J. Burke, F. J. Rich, and M. Smiddy (1981), Quantitative simulation of a magnetospheric substorm. I. Model logic and overview, *J. Geophys. Res.*, **86**, 2217–2241, doi:10.1029/JA086iA04p02217.
- Hedin, A. E. (1991), Extension of the MSIS thermospheric model into the middle and lower atmosphere, *J. Geophys. Res.*, **96**, 1159–1172, doi:10.1029/90JA02125.
- Henderson, M. G., G. D. Reeves, H. E. Spence, R. B. Sheldon, A. M. Jorgensen, J. B. Blake, and J. F. Fennell (1997), First energetic neutral atom images from POLAR, *Geophys. Res. Lett.*, **24**, 1167–1170, doi:10.1029/97GL01162.
- Hodges, R. R., Jr. (1994), Monte Carlo simulation of the terrestrial hydrogen exosphere, *J. Geophys. Res.*, **99**, 23,229–23,247, doi:10.1029/94JA02183.
- Horwitz, J. L., C. R. Baugher, C. R. Chappell, E. G. Shelley, and D. T. Young (1982), Conical pitch angle distributions of very low-energy ion fluxes observed by ISEE 1, *J. Geophys. Res.*, **87**, 2311–2320, doi:10.1029/JA087iA04p02311.
- Keller, K., M.-C. Fok, A. Narock, M. Hesse, L. Rastaetter, M. M. Kuznetsova, T. I. Gombosi, and D. L. DeZeeuw (2005), Effect of multiple substorms on the buildup of the ring current, *J. Geophys. Res.*, **110**, A08202, doi:10.1029/2004JA010747.
- Kozyra, J. U., M. W. Liemohn, C. R. Clauer, A. J. Ridley, M. F. Thomsen, J. E. Borovsky, J. L. Roeder, V. K. Jordanova, and W. D. Gonzalez (2002), Multistep *Dst* development and ring current composition changes during the 4–6 June 1991 magnetic storm, *J. Geophys. Res.*, **107**(A8), 1224, doi:10.1029/2001JA000023.
- Lennartsson, W., and R. D. Sharp (1982), A comparison of the 0.1–17 keV/e ion composition in the near equatorial magnetosphere between quiet and disturbed conditions, *J. Geophys. Res.*, **87**, 6109–6120, doi:10.1029/JA087iA08p06109.
- Lennartsson, W., R. D. Sharp, E. G. Shelley, R. G. Johnson, and H. Balsiger (1981), Ion composition and energy distribution during 10 magnetic storms, *J. Geophys. Res.*, **86**, 4628–4638, doi:10.1029/JA086iA06p04628.
- Mauk, B. H., and C. E. McIlwain (1975), UCSD auroral particles experiment, *IEEE Trans. Aerosp. Electron. Syst.*, **AES-11**, 1125–1130, doi:10.1109/TAES.1975.308164.
- Mauk, B. H., and C.-I. Meng (1983), Characterization of geostationary particle signatures based on the “injection boundary” model, *J. Geophys. Res.*, **88**, 3055–3071, doi:10.1029/JA088iA04p03055.
- Mauk, B. H., and C.-I. Meng (1986), Macroscopic ion acceleration associated with the formation of the ring current in the earth's magnetosphere, in *Ion Acceleration in the Magnetosphere and Ionosphere*, *Geophys. Monogr. Ser.*, vol. 38, edited by T. Chang, pp. 351–361, AGU, Washington, D. C.
- McComas, D. J., P. W. Valek, J. L. Burch, C. J. Pollock, R. M. Skoug, and M. F. Thomsen (2002), Filling and emptying of the plasma sheet: Remote observations with 1–70 keV energetic neutral atoms, *Geophys. Res. Lett.*, **29**(22), 2079, doi:10.1029/2002GL016153.

- McComas, D. J., et al. (2009), The Two Wide-angle Imaging Neutral-atom Spectrometers (TWINS) NASA Mission-of-Opportunity, *Space Sci. Rev.*, **142**, 157–231, doi:10.1007/s11214-008-9467-4.
- McFadden, J. P., C. W. Carlson, D. Larson, M. Ludlam, R. Abiad, B. Elliott, P. Turin, M. Marckwardt, and V. Angelopoulos (2008), The THEMIS ESA plasma instrument and in-flight calibration, *Space Sci. Rev.*, **141**, 277–302, doi:10.1007/s11214-008-9440-2.
- McIlwain, C. E. (1972), Plasma convection in the vicinity of the geosynchronous orbit, in *Earth's Magnetospheric Processes*, edited by B. M. McCormac, pp. 268–279, Reidel, Dordrecht, Netherlands.
- Mitchell, D. G., et al. (2000), High energy neutral atom (HENA) imager for the IMAGE mission, *Space Sci. Rev.*, **91**, 67–112, doi:10.1023/A:1005207308094.
- Mitchell, D. G., P. C. Brandt, E. C. Roelof, D. C. Hamilton, K. Retterer, and S. Mende (2003), Global imaging of O⁺ from IMAGE/HENA, *Space Sci. Rev.*, **109**, 63–75, doi:10.1023/B:SPAC.0000007513.55076.00.
- Moore, T. E., M.-C. Fok, D. C. Delcourt, S. P. Slinker, and J. A. Fedder (2008), Plasma plume circulation and impact in an MHD substorm, *J. Geophys. Res.*, **113**, A06219, doi:10.1029/2008JA013050.
- Nagai, T., J. F. E. Johnson, and C. R. Chappell (1983), Low-energy (<100 eV) ion pitch angle distributions in the magnetosphere by ISEE 1, *J. Geophys. Res.*, **88**, 6944–6960, doi:10.1029/JA088iA09p06944.
- Østgaard, N., S. B. Mende, H. U. Frey, G. R. Gladstone, and H. Lauche (2003), Neutral hydrogen density profiles derived from geocoronal imaging, *J. Geophys. Res.*, **108**(A7), 1300, doi:10.1029/2002JA009749.
- Pollock, C. J., et al. (2000), Medium energy neutral atom (MENA) imager for the IMAGE mission, *Space Sci. Rev.*, **91**, 113–154, doi:10.1023/A:1005259324933.
- Pollock, C. J., et al. (2003), The role and contributions of energetic neutral atom (ENA) imaging in magnetospheric substorm research, *Space Sci. Rev.*, **109**, 155–182, doi:10.1023/B:SPAC.0000007518.93331.d5.
- Rairden, R. L., L. A. Frank, and J. D. Craven (1986), Geocoronal imaging with Dynamics Explorer, *J. Geophys. Res.*, **91**, 13,613–13,630, doi:10.1029/JA091iA12p13613.
- Reeves, G. D., and M. G. Henderson (2001), The storm-substorm relationship: Ion injections in geosynchronous measurements and composite energetic neutral atom images, *J. Geophys. Res.*, **106**, 5833–5844, doi:10.1029/2000JA003017.
- Riley, P. (1994), *Electrodynamics of the low-latitude ionosphere*, Ph.D. thesis, Rice Univ., Houston, Tex.
- Roelof, E. C. (1987), Energetic neutral atom image of a storm-time ring current, *Geophys. Res. Lett.*, **14**, 652–655, doi:10.1029/GL014i006p00652.
- Roelof, E. C. (1997), ENA emission from nearly mirroring magnetospheric ions interacting with the exosphere, *Adv. Space Res.*, **20**, 361–366, doi:10.1016/S0273-1177(97)00692-3.
- Roelof, E. C., and D. J. Williams (1988), The terrestrial ring current: From in situ measurements to global images using energetic neutral atoms, *Johns Hopkins APL Tech. Dig.*, **9**, 144–163.
- Roelof, E. C., D. G. Mitchell, and D. J. Williams (1985), Energetic neutral atoms (E ~ 50 keV) from the ring current: IMP 7/8 and ISEE 1, *J. Geophys. Res.*, **90**, 10,991, doi:10.1029/JA090iA11p10991.
- Scime, E. E., A. M. Keesee, J.-M. Jahn, J. L. Kline, C. J. Pollock, and M. Thomsen (2002), Remote ion temperature measurements of Earth's magnetosphere: Medium energy neutral atom (MENA) images, *Geophys. Res. Lett.*, **29**(10), 1438, doi:10.1029/2001GL013994.
- Shelley, E. G., D. M. Klumpp, W. K. Peterson, A. Ghielmetti, H. Balsiger, J. Geiss, and H. Rosenbauer (1985), AMPTE/CCE observations of the plasma composition below 17 keV during the September 4, 1984 magnetic storm, *Geophys. Res. Lett.*, **12**, 321, doi:10.1029/GL012i005p00321.
- Sibeck, D. G., and V. Angelopoulos (2008), THEMIS science objectives and mission phases, *Space Sci. Rev.*, **141**, 35–59, doi:10.1007/s11214-008-9393-5.
- Smith, P. H., and R. A. Hoffman (1974), Direct observation in the dusk hours of the characteristics of the storm time ring current particles during the beginning of magnetic storms, *J. Geophys. Res.*, **79**, 966–971, doi:10.1029/JA079i007p00966.
- Tsyganenko, N. A. (1995), Modeling the Earth's magnetospheric magnetic field confined within a realistic magnetopause, *J. Geophys. Res.*, **100**, 5599–5612, doi:10.1029/94JA03193.
- Tsyganenko, N. A., and T. Mukai (2003), Tail plasma sheet models derived from Geotail particle data, *J. Geophys. Res.*, **108**(A3), 1136, doi:10.1029/2002JA009707.
- Tsyganenko, N. A., and D. P. Stern (1996), Modeling the global magnetic field of the large-scale Birkeland current systems, *J. Geophys. Res.*, **101**, 27,187–27,198, doi:10.1029/96JA02735.
- Valek, P., P. C. Brandt, N. Buzulukova, M.-C. Fok, J. Goldstein, D. J. McComas, J. D. Perez, E. Roelof, and R. Skoug (2010), Evolution of low-altitude and ring current ENA emissions from a moderate magnetospheric storm: Continuous and simultaneous TWINS observations, *J. Geophys. Res.*, **A11209**, doi:10.1029/2010JA015429.
- Vallat, C., et al. (2004), First comparisons of local ion measurements in the inner magnetosphere with energetic neutral atom magnetospheric image inversions: Cluster-CIS and IMAGE-HENA observations, *J. Geophys. Res.*, **109**, A04213, doi:10.1029/2003JA010224.
- Weimer, D. R. (2001), An improved model of ionospheric electric potentials including substorm perturbations and applications to the Geospace Environment Modeling November 24, 1996, event, *J. Geophys. Res.*, **106**, 407–416, doi:10.1029/2000JA000604.
- Wolf, R. A. (1974), Calculations of magnetospheric electric fields, in *Magnetospheric Physics*, edited by B. M. McCormac, pp. 167–177, D. Reidel, Dordrecht, Netherlands.
- Wolf, R. A., R. W. Spiro, S. Sazykin, and F. R. Toffoletto (2007), How the Earth's inner magnetosphere works: An evolving picture, *J. Atmos. Sol. Terr. Phys.*, **69**, 288–302, doi:10.1016/j.jastp.2006.07.026.
- Zaharia, S. V., V. K. Jordanova, M. F. Thomsen, and G. D. Reeves (2006), Self-consistent modeling of magnetic fields and plasma in the inner magnetosphere: Application to a geomagnetic storm, *J. Geophys. Res.*, **111**, A11S14, doi:10.1029/2006JA011619.
- Zoennchen, J. H., U. Nass, G. Lay, and H. J. Fahr (2010), 3-D-Geocoronal hydrogen density derived from TWINS Ly- α -data, *Ann. Geophys.*, **28**, 1221–1228, doi:10.5194/angeo-28-1221-2010.

N. Buzulukova, S.-H. Chen, and M.-C. Fok, NASA Goddard Space Flight Center, Greenbelt, MD 20771, USA. (mei-ching.h.fok@nasa.gov)
J. Goldstein, D. J. McComas, and P. W. Valek, Southwest Research Institute, San Antonio, TX 78228, USA.